Journal of ELECTRONIC MATERIALS, Vol. 41, No. 6, 2012
DOI: 10.1007/s11664-011-1894-4

Thermoelectric Energy Harvesting from Transient Ambient Temperature Gradients

ANDRÉ MOSER,[1,3] METIN ERD,[2] MILOS KOSTIC,[2] KEITH COBRY,[1] MICHAEL KROENER,[1] and PETER WOIAS[1]

1.—Laboratory for Design of Microsystems, Department of Microsystems Engineering – IMTEK, University of Freiburg, Georges-Koehler-Allee 102, 79110 Freiburg, Germany. 2.—Laboratory for Electrical Instrumentation, Department of Microsystems Engineering – IMTEK, University of Freiburg, Georges-Koehler-Allee 103, 79110 Freiburg, Germany. 3.—e-mail: andre.moser@imtek.de

We examine a thermoelectric harvester that converts electrical energy from the naturally occurring temperature difference between ambient air and large thermal storage capacitors such as building walls or the soil. For maximum power output, the harvester design is implemented in two steps: *source matching* of the thermal and electrical interfaces to the energy source (system level) followed by *load matching* of the generator to these interfaces (subsystem level). Therefore, we measure thermal source properties such as the temperature difference, the air velocity, and the cutoff frequency in two application scenarios (road tunnel and office building). We extend a stationary model of the harvester into the time domain to account for transient behavior of the source. Based on the model and the source measurements, we perform the source and load matching. The resulting harvester consists of a pin fin heat sink with a thermal resistance of 6.2 K/W and a cutoff frequency 2.5 times greater than that of the source, a thermoelectric generator, and a DC/DC step-up converter starting at a total temperature difference of only ΔT = 1.2 K. In a final road tunnel field test, this optimized harvester converts 70 mJ of electrical energy per day without any direct solar irradiation. The energy provided by the harvester enables 415 data transmissions from a wireless sensor node per day.

Key words: Thermoelectric harvester, ambient temperature gradient, transient, source matching, load matching, energy-autonomous wireless sensor node

INTRODUCTION

Wireless sensor networks (WSN) represent an emerging technology, used for instance in structural health monitoring (SHM) of infrastructure such as buildings, tunnels, and bridges or in traffic surveillance.[1] Supplying power to such highly distributed networks, especially at remote locations, is a big challenge because power grids are costly to install and batteries offer only a limited lifetime. Energy harvesting, by contrast, provides a reliable and *in-situ* power supply based on the conversion of ambient into electrical energy.[2] An omnipresent ambient energy source is thermal energy: Ambient air heats up during the day due to solar irradiation and cools down at night. This periodic temperature variation of the air transfers to any solid in contact. The temperature variation of the solid is dampened by its thermal inertia, thus creating a temperature difference between ambient air and the solid.

A thermoelectric generator (TEG) is able to directly convert thermal into electrical energy when placed between ambient air and a solid such as a building wall or the soil. A complete thermoelectric harvester consists of thermal interfaces to the air and the solid, a TEG, and an electrical interface (load). The power output of the harvester depends on the energy source and the harvester components.

(Received July 31, 2011; accepted December 22, 2011; published online February 10, 2012)

Relevant source properties to determine this power output are the total temperature difference $\Delta T = T_{air} - T_{wall}$ and the radiative, convective, and conductive heat transfer at the air and wall interfaces. If these source properties are known, the thermal/electrical interfaces of the harvester must be designed appropriately, which is what we call *source matching*. The TEG must then be thermally[3,4] and electrically[5] adapted to these thermal/electrical interfaces. This *load matching* is the second step to ensure maximum power output of the harvester.

A thermoelectric harvester that uses the temperature difference between ambient air and wall has not been presented in the literature yet. Only two publications refer to air/soil harvesters similar to our air/wall harvester. Two differences should be noted: (1) The thermal energy available from the soil is greater than from a building wall of fixed orientation, because the soil receives direct solar irradiation the whole day, whereas the northeast wall used in our study receives only 1–3 h; (2) Both cited publications solely harvest energy, but do not use the energy to demonstrate the feasibility of a thermoelectrically powered WSN.

In 2002, Lawrence and Snyder[6] built a harvester consisting of a plate fin heat sink as the air interface, a micro-TEG, and a finned heat pipe as the soil interface, buried in the ground. Although the complete harvester was introduced, only the soil interface was characterized in a field test. Another major drawback of this work is that the total temperature difference between air and soil is not presented. Hence, the quality of the thermal interfaces cannot be judged, except for the heat pipe: The authors state that "most of the temperature drop in the system was across the heat pipe—up to 4.5 K out of the 10 K total across the air and soil." The heat pipe had to work against gravity during daytime, which resulted in a large temperature drop. The authors claim that source matching at the air interface may be neglected, and they disregard convective and radiative heat transfer at the air interface. Consequently, they employ a plate fin heat sink, which is not well matched to the source, as we will show.

Meydbray et al.[7] present a thermoelectric harvester consisting of an enlarged TEG ceramic plate as the air interface, the TEG, and a large copper plate as the soil interface. The authors introduce an analytical model based on heat conduction, heat convection, and Peltier heat. Time dependencies between harvester and source are not considered. Radiative heat transfer is neglected, even though the authors state that solar irradiation significantly contributes to the power output. A load-matching condition is derived from the model (optimum thermoleg length) but is not used for the harvester layout in the field test. The greatest influence on the power output originates from the air interface. Consequently, most power is achieved for the harvester with the smallest thermal resistance of the air interface, yielding average power of 575 μW and energy of 49.7 J per day. However, again, the total temperature difference is not recorded, preventing qualitative analysis of the thermal interfaces. A comparison of the different harvesters based on the field measurements is difficult since the measurements were executed consecutively, which means under different weather conditions (i.e., cloudy, sunny, etc.).

This paper is organized as follows: The properties of the thermal interface, the TEG, and the electrical interface are introduced and summed up in a transient model of the complete harvester. Then, the properties of the thermal energy source are presented in two simultaneous field measurements in the tunnel and at the building. The thermal and electrical interfaces are matched to the determined source properties (*source matching*) and verified by laboratory measurements, simulations, and analytical means. Then, the TEG is matched to these thermal and electrical loads (*load matching*). Finally, the source- and load-matched harvester is able to power a WSN in a tunnel field measurement.

MODELING OF THE HARVESTER PROPERTIES

Thermal Interface

The thermal interfaces connect the TEG to the heat source (air) and sink (wall), thus determining how much energy enters the TEG. The corresponding thermal interface resistances must be matched to the source and the TEG to prevent power loss. As the TEG is in direct contact with the wall, the wall interface is a solid–solid interface with negligibly small thermal resistance. The air interface, by contrast, depends on the fluid properties of air, which is a good thermal isolator.[8] Hence, reduction of the air interface resistance is of paramount importance. In low-power applications, as encountered here, only passive heat sinks can be afforded as the air interface. The thermal resistance

$$K = \frac{1}{h \cdot A} \tag{1}$$

of such a heat sink results from the heat transfer coefficient h and the surface area A in contact with the air ($A = A_t - A_g$ = total surface area − area covered by the TEG).[8] To compare heat sinks of different size, it is not appropriate to use the absolute thermal resistance given by Eq. 1, since a larger heat sink will have a smaller thermal resistance. Therefore, we define a relative measure for the thermal resistance, which we call the dimensionless *surface density*

$$S = \frac{A_t}{A_{base}}. \tag{2}$$

S is the ratio of the total surface area A_t of a heat sink to its base plate area A_{base}. The surface density is comparable to the thermal resistance per area but offers the advantage of being independent of the

heat transfer coefficient, since it is a purely geometric quantity. S is directly proportional to the quality of the thermal interface. However, this concept only works if the flow between the fins of a heat sink remains unaffected (h = const.). Therefore, the fin distance must be greater than twice the convective boundary layer thickness

$$\delta = \frac{5}{\sqrt{\frac{v}{\nu_k \cdot x}}}. \tag{3}$$

For a flat plate δ depends on the velocity v, the kinematic viscosity ν_k, and the fin length x.[8] The thermal capacitance

$$C = c_{vol} \cdot V \tag{4}$$

is the product of the volume-specific heat capacity c_{vol} and the volume V.[8] It represents the thermal inertia and thus the dynamic behavior of the heat sink. By combining Eq. 1 and Eq. 4, the cutoff frequency f_c of the heat sink is yielded as

$$f_c = \frac{1}{K \cdot C} = \frac{h \cdot A}{c_{vol} \cdot V}. \tag{5}$$

f_c is a measure of the ability to follow a transient temperature signal.

Transient Harvester Model

A thermal network modeling an air–soil harvester has been introduced by Meydbray et al.[7] We extend this stationary model with a thermal capacitance to account for transient behavior of the heat sink (Fig. 1). The thermal capacitance of the TEG is not considered here, because it is negligibly small compared to the heat sink (factor of 14.7 between the ickpen45w and the 128A0020 in Table IV). Joule and Thompson heat flows may be neglected for $\Delta T < 10$ K.[5,9] Direct solar irradiation is not considered, as it has only a minor influence in the chosen application sites (tunnel wall, northeast building wall).

The heat flows q in the center node of Fig. 1 are given by

$$\frac{T_{air} - T_1}{K} = C \cdot \dot{T}_1 + \frac{T_1 - T_{wall}}{K_g} + \frac{\alpha_g^2 \left(T_1^2 - T_1 T_{wall}\right)}{R_g + R}, \tag{6}$$

with air, center, and wall temperatures T_{air}, T_1, and T_{wall}, thermal resistance K and capacitance C of the heat sink (thermal load), electrical load resistance R, and thermal resistance K_g, electrical resistance R_g, and Seebeck coefficient α_g of the TEG. In Fig. 1 T_{wall} is accessed underneath the harvester, thus already including all heat flows (q_P and q_3) at the wall. Equation 6 is a nonlinear differential equation due to T_1^2 in the Peltier heat flow. Linearization of T_1 is necessary to enable an analytical solution. Therefore, T_1 is factored out in the Peltier heat flow

$$\frac{\alpha_g^2 T_1 (T_1 - T_{wall})}{R_g + R} \approx \frac{\alpha_g^2 T_0 (T_1 - T_{wall})}{R_g + R} \tag{7}$$

and approximated by the mean air temperature T_0. This approximation introduces a maximum error of [+1.5% | −0.8%] in the temperature difference ΔT_g at the TEG (worst-case approx.: ΔT = [+10 K | −10 K], and T_0, K, R, K_g, R_g, and α_g taken from Table IV). Separation of the total temperature difference $\Delta T = T_{air} - T_{wall}$ from the TEG temperature difference $\Delta T_g = T_1 - T_{wall}$ and use of Eq. 5 yield

$$\Delta T = \left(1 + \frac{K}{K_g} + \frac{\alpha_g^2 T_0 K}{R_g + R}\right) \Delta T_g + \frac{1}{f_c} \cdot \Delta \dot{T}_g. \tag{8}$$

This linear differential equation can be solved by separation of variables. With the initial condition $\Delta T_g(t = 0) = 0$, the solution for a ΔT step is

$$\Delta T_g(t) = \frac{\Delta T}{1 + \frac{K}{K_g} + \frac{\alpha_g^2 T_0 K}{R_g + R}} \cdot \left(1 - e^{-t \cdot f_c \cdot \left(1 + \frac{K}{K_g} + \frac{\alpha_g^2 T_0 K}{R_g + R}\right)}\right). \tag{9}$$

The first term in Eq. 9 represents the DC value of ΔT_g as known from literature.[5] The second term shows the exponential time dependence of ΔT_g due to the thermal low-pass filtering of the heat sink. Since the real ΔT is a periodic function, we use a Fourier transformation of Eq. 8 to obtain the transfer function of the harvester

$$\Delta T_g(f) = \frac{\Delta T}{1 + \frac{K}{K_g} + \frac{\alpha_g^2 T_0 K}{R_g + R} + j \cdot \frac{f}{f_c}}. \tag{10}$$

With Eq. 9 and Eq. 10 we are able to calculate the TEG temperature difference ΔT_g from a known total temperature difference ΔT. The output power of the TEG is

$$P = \left(\frac{\alpha_g \Delta T_g}{R_g + R}\right)^2 \cdot R. \tag{11}$$

Now combining Eq. 9 and Eq. 11, the step response of the output power becomes

$$P(t) = \left(\frac{\alpha_g \Delta T}{1 + \frac{K}{K_g} + \frac{\alpha_g^2 T_0 K}{R_g + R}}\right)^2 \cdot \left(1 - e^{-t \cdot f_c \cdot \left(1 + \frac{K}{K_g} + \frac{\alpha_g^2 T_0 K}{R_g + R}\right)}\right)^2 \cdot \frac{R}{(R_g + R)^2}. \tag{12}$$

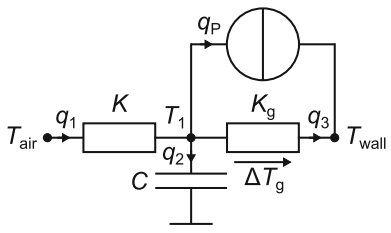

Fig. 1. Thermal equivalent network of the thermoelectric harvester.

In steady state ($t \rightarrow \infty$), the exponential term in Eq. 12 vanishes and the output power $P(t)$ solely depends on the temperature and voltage dividers. However, problems occur in the transient state ($t \rightarrow 0$) where a step response of the output power is delayed depending on the cutoff frequency f_c of the heat sink. Thus, an increase of the cutoff frequency ($f_{c1} \rightarrow f_{c2}$) shortens the time delay and increases the output power (Fig. 2).

FIELD MEASUREMENT OF THE SOURCE PROPERTIES

The ambient temperature gradient is defined by three physical properties:

1. Temperature difference amplitude $\Delta T = T_{air} - T_{wall}$
2. Dependence of the temperature difference on time t (steady versus transient state)
3. Heat transfer modes at the air/wall interfaces represented by the heat transfer coefficient h

If one of these properties is neglected, this will result in a mismatch between harvester and source followed by power loss. Therefore, field measurements were performed at two application sites to determine these source properties.

Measurement Setup and Locations

Two field measurements of the ambient temperature gradient were performed simultaneously during 19 to 24 May 2011 in a traffic tunnel (Hugenwald road tunnel, 15 km northeast of Freiburg, Germany) and at the outer wall of a building (office building, northeast orientation, Freiburg, Germany). The two measurements were run in parallel to ensure similar weather conditions. A data logger (LE-LOG_1623_USB_TE_SP, LeTe) was used with Pt1000 temperature sensors and a hot-wire anemometer at a sampling rate of 5 s (Table I).

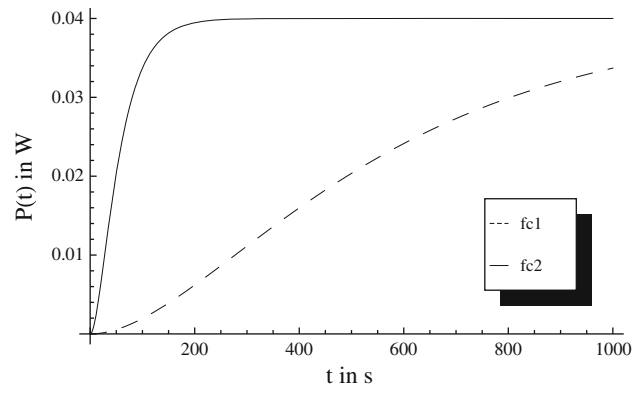

Fig. 2. Step responses of the output power (Eq. 12) to a temperature step of 1 K. The heat sink cutoff frequency f_{c2} (solid line) is ten times greater than f_{c1} (dashed line), which significantly increases the output power for short-term temperature variations.

Ambient Temperature Gradient Amplitude ΔT

The ambient temperature gradient resembles a sine function with base period of 24 h at both locations (Fig. 3). The amplitude in the tunnel ($|\Delta T|_{mean}$ = 1.2 K) is a factor of 2 smaller than at the building ($|\Delta T|_{mean}$ = 2.2 K). In the tunnel, the large thermal mass of the surrounding ground and the distance to the outside lead to large thermal dampening (Fig. 3). Air and wall even become isothermal in the center of long tunnels (≥5 km). Since direct solar irradiation is not present, the tunnel represents a worst-case scenario for a thermal harvester. Solar irradiation on the building wall was only present between 07:00 and 10:00 yet causing spikes of 6 K to 10 K in ΔT (Fig. 3).

Convective Heat Transfer

Measurements of the air velocity at 40 mm distance to the wall indicate forced convection

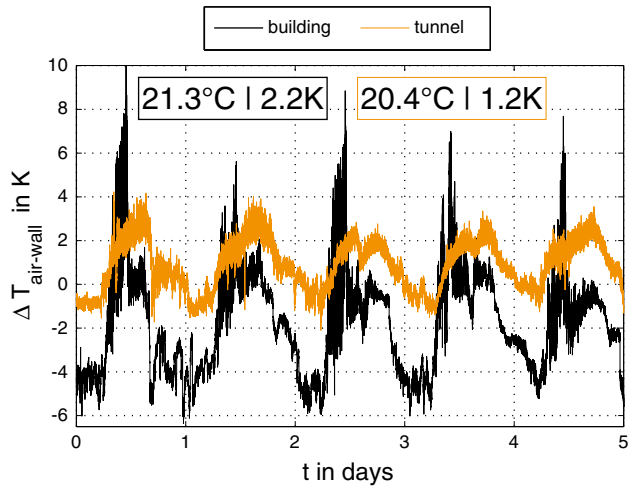

Fig. 3. Total temperature difference ΔT between air (40 mm wall distance) and wall (on the wall surface) measured at a building in Freiburg and in the Hugenwald road tunnel (depth of 303 m), 15 km northeast of Freiburg, Germany. The numbers in the box show the mean air temperature T_0 (°C) and the absolute mean of the temperature difference $|\Delta T|_{mean}$ (K), respectively.

Table I. Temperature and airflow sensors used for field and laboratory measurements

Quantity	Sensor	Model, Company	Resolution	Position
T_{air}	Pt1000	M222, Heraeus	1.4 mK	40 mm wall distance
T_{wall}	Pt1000	M222, Heraeus	1.4 mK	On the wall surface
v_{air}	Hot-wire anemometer	RLSW8AL, Seikom Electronic	0.05 m/s	40 mm wall distance

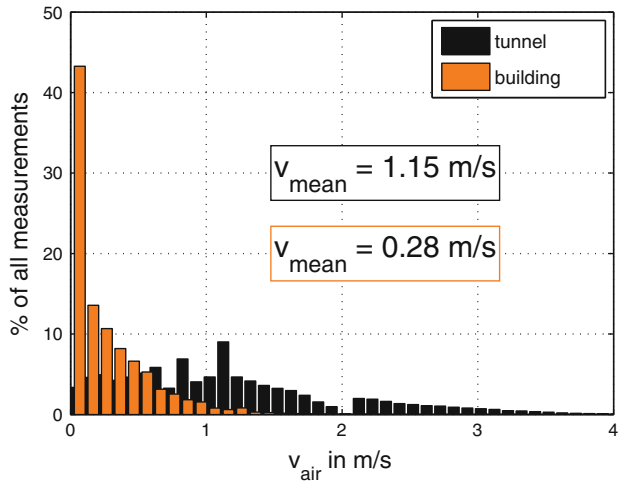

Fig. 4. Air flow at 40 mm wall distance in the tunnel and building field measurements.

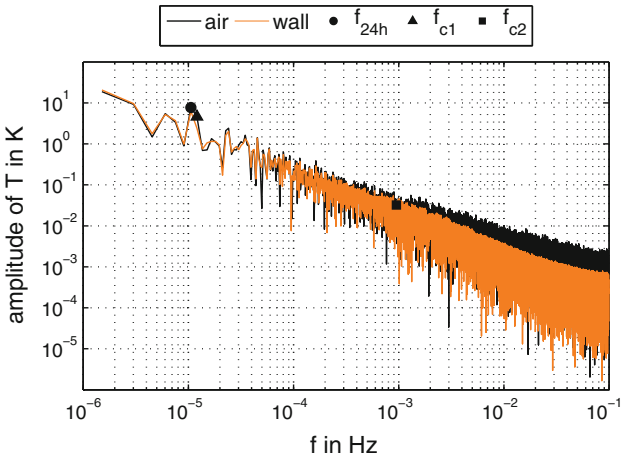

Fig. 5. Frequency spectrum of the air and wall temperature signals in the building measurement. The marked frequencies correspond to the day period ($f_{24h} \approx 11.6\ \mu$Hz) and the cutoff frequencies of the wall determined by the 3 dB limit ($f_{c1} \approx 12.1\ \mu$Hz) and the separation point of the two spectrums ($f_{c2} \approx 1$ mHz).

conditions in the tunnel and at the building (Fig. 4). The mean air velocity v_{mean} in the tunnel is approximately four times greater than at the building wall (1.15/0.28 ≈ 4.1). This is due to vehicles that pass through the tunnel, generating a so-called traffic-induced airflow. The air velocity at the outer building wall is close to natural convection with 43% of the measured values below 0.15 m/s.

Time Dependence of ΔT

The total temperature difference $\Delta T = T_{air} - T_{wall}$ results from the difference between the air and wall temperatures. The frequency spectrum is calculated separately for T_{air} and T_{wall} at the building to show the thermal dampening of the wall (Fig. 5). Both temperature signals are broadband with frequencies of approx. 1 μHz up to 0.1 Hz. The most power is

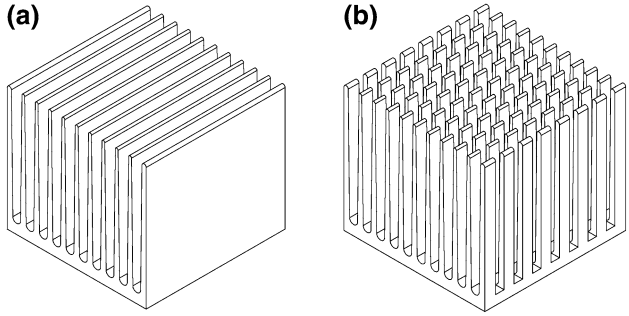

Fig. 6. Thermal interfaces (heat sinks) connecting the harvester to the air: (a) plate fin heat sink Fischer sk475, 50 mm × 50 mm × 45 mm, fin width 50 mm, mean fin spacing 3.35 mm, anodized aluminum; (b) pin fin heat sink Fischer ickpen45w, 50 mm × 50 mm × 45 mm, fin width 3.56 mm, anodized aluminum.

available in the low frequencies, most evidently in the 24-h base period ($f_{24h} \approx 11.6\ \mu$Hz). The large thermal inertia of the wall represents a thermal low-pass filter to the air temperature. The cutoff frequency of the wall surface f_{c1} is consequently calculated from a 3 dB drop in the transfer function T_{wall}/T_{air}, yielding approx. 12.1 μHz. This value is much too high and is a result of the discretization into 65,536 frequencies in the Fast Fourier Transform (FFT). The 3 dB limit is therefore marked as a separation point between the two Bode plots given by $f_{c2} \approx 1$ mHz in Fig. 5. A detailed thermal model of the wall has to be derived in the future to assess this frequency properly.

SOURCE MATCHING—THERMAL INTERFACE

General Design Considerations

The thermal interface of the harvester is influenced by the convective heat transfer (air velocity v_{air}) and the time dependence (cutoff frequency f_c) of the source. The thermal interface must have a greater cutoff frequency than the wall $f_{c2} \approx 1$ mHz to convert energy from the source. According to Eq. 5 and Eq. 12 the thermal resistance and capacitance need to be reduced to achieve this goal.

The thermal resistance of a heat sink is reduced as its surface density is increased (Eq. 2). For this purpose, the surface density of 900 passive commercial heat sinks was compared. The plate fin heat sink sk475 and the pin fin heat sink ickpen45w from Fischer achieved the greatest values with $S_{sk475} = 20.6$ and $S_{ickpen45w} = 17.2$. The boundary layer thickness calculated from the fin width of both heat sinks via Eq. 3 suggests using the ickpen45w to not impede the airflow. The source-matched heat sinks are depicted in Fig. 6, and their thermal properties S, δ, K, C, and f_c are listed in Table II.

The reduction of the thermal capacitance depends on the volume of the heat sink and the volume-specific heat capacity of the material (Eq. 4). Therefore, aluminum ($c_{vol,Al} = 2260$ J/m^{3}K) is preferred to

Table II. Surface density S, boundary layer thickness δ, mean thermal resistance K, thermal capacitance C, and mean cutoff frequency f_c of the thermal interfaces matched to the sources air/building (bld) and air/tunnel (tnl) ambient temperature gradient

	S –	δ mm	K K/W	K K/W	C J/K	f_c mHz	f_c mHz
ickpen45w	17.2	1.1	6.2	3.2	66.3	2.5	4.8
sk475	20.6	4.1	10.6	3.4	100.8	0.9	3
v_{air} in m/s	–	1	0.28	1.15	–	0.28	1.15
Thermal source	–	–	bld	tnl	–	bld	tnl

copper ($c_{vol,Cu}$ = 3414 J/m^{3}K).[10] The fin profile occupying the least volume is the so-called concave parabolic profile.[8] Because of fabrication restrictions, the concave parabolic profile is approximated by a triangular profile used for both heat sinks. Additional volume reduction is possible by cross-cutting the plate fins into pin fins. With a sawing gap of 3 mm, the ickpen45w (Fig. 6 b) saves 34% of volume compared with the sk475.

Simulation of the Heat Transfer Coefficient

The heat transfer coefficient of the sk475 and ickpen45w heat sinks strongly depends on fluid dynamics: 73.1% of the total heat flow through the heat sink base (v_{air} = 1 m/s, ickpen45w) originates from forced convection as calculated by the following simulation (24.4% ambient radiation, 2.5% natural convection): A thermal-fluid simulation of the heat sinks in the wind channel (without TEG) was done in ANSYS Icepak. The boundary conditions were T_{wall} = 21°C and T_{air} = 20°C at airflow velocities of v_{air} = 0.5 m/s to 2 m/s. The heat transfer coefficient

$$h_{simulation} = \frac{q_{base} A_{base}}{\Delta T (A_t - A_{base})} \tag{13}$$

was calculated from the heat flux through the heat sink base q_{base}, the total surface area A_t, the base area A_{base}, and the temperature difference ΔT and is shown in Fig. 8.

Measurement of the Heat Transfer Coefficient

The convective heat transfer coefficient of the sk475 and ickpen45w heat sinks was measured in a wind channel (Fig. 7) with the data acquisition system introduced in Table I. The total temperature difference ΔT between air (room temperature) and wall (heat exchanger) was set to −5 K. The air velocity was varied between 0.5 m/s and 2 m/s. The heat transfer coefficient h of the thermal interface was calculated by

$$h = \left(K_g \left(\frac{\alpha_g}{U_g} \Delta T - 1 \right) \cdot (A_t - A_g) \right)^{-1} \tag{14}$$

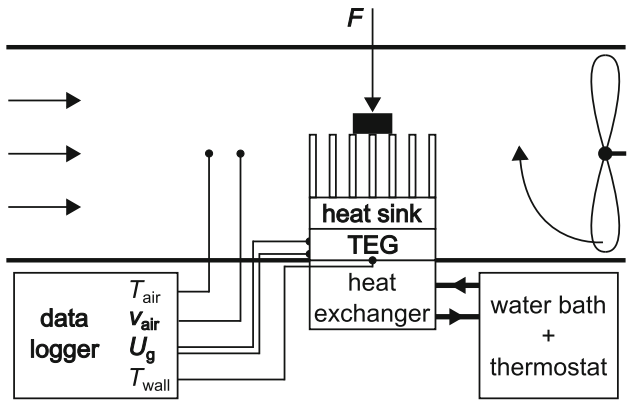

Fig. 7. Wind channel setup to determine the thermal resistance and the cutoff frequency of the heat sinks via the heat transfer coefficient.

with the index "g" indicating the TEG's thermal resistance K_g, Seebeck coefficient α_g, voltage U_g, and base area A_g.

The heat transfer coefficients for both heat sinks are depicted in Fig. 8. The pin fin heat sink ickpen45w offers better heat transfer than the plate fin heat sink, especially at low air velocities as has also been shown in Ref. 9. The flat-plate approximation (Eq. 3) was used as an analytical model with fin widths of 3.625 mm (ickpen45w) and 50 mm (sk475). As the boundary layer thickness is inversely proportional to the heat transfer, the ickpen45w fin (Fig. 8, a ick45) yields a greater heat transfer coefficient than the sk475 fin (Fig. 8, a sk475). In general, a free-standing fin (Fig. 8, analytical) transfers heat better than a fin in an array (Fig. 8, simulation), because the airflow on inner pins is reduced by surrounding pins. These air flow restrictions of adjacent fins in an array are typically determined by simulation and measurement. The simulation yields the correct trend, but the h values are too large (Fig. 8, simulation) compared with the measurement (Fig. 8, measurement). In the simulation a rectangular fin profile must be used to allow meshing; the real heat sinks employ a triangular profile with curvatures at the tip and the base. Moreover, the simulation does not consider contact resistances and assumes a homogeneous flow profile, whereas, in the measurement, the exact flow profile is unknown.

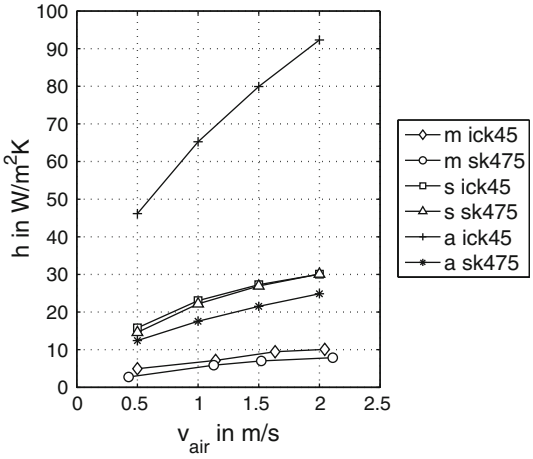

Fig. 8. Measured (m), simulated (s), and analytically derived (a) heat transfer coefficient *h* of the thermal interfaces ickpen45w and sk475.

The thermal resistance K and the cutoff frequency f_c are proportional to the heat transfer coefficient in Eq. 1 and Eq. 5. The values for K and f_c depend on the source property v_{air}, which was determined in the source field measurements (Fig. 4). Hence, K and f_c are determined for the mean air velocities 0.28 m/s and 1.15 m/s, respectively (Table II). The pin fin heat sink ickpen45w yields a smaller thermal resistance and a greater cutoff frequency than the plate fin heat sink sk475 (Table II). The ickpen45w is therefore employed as air interface.

SOURCE MATCHING—ELECTRICAL INTERFACE

In both application scenarios, the ambient temperature gradient is a low-energy source offering a mean absolute temperature difference of 1.2 K to 2.2 K. Consequently, the resulting TEG output voltage will be in the mV range. A DC/DC step-up converter is necessary to generate a voltage level sufficient to power an electronic device. For low-voltage sources, the primary goal is to reduce the startup voltage $U_{startup}$ of this converter as much as possible.[11] If the TEG output voltage is smaller than the startup voltage, no energy is converted and the sensor node cannot operate. As the polarity of the temperature difference changes, the DC/DC step-up converter should be able to boost positive and negative TEG voltages. The converter with the lowest startup voltage is currently the ECT310 starting at 15 mV (Table III). This converter is therefore employed as the electrical interface. A drawback of this converter is that it only works for positive polarity. The LTC3109 is a bipolar converter but starts only from 30 mV (Table III).

LOAD MATCHING—TEG

Load matching states that maximum power is drawn from a system when the internal and external loads are equal. Hence, the TEG must be matched to its thermal load K and its electrical load R. As the Peltier effect alternates the internal resistances K_g and R_g of the TEG during operation, the load-matching conditions are

$$K_g = K\sqrt{1+ZT_0} \tag{15}$$

and

$$R_g = \frac{R}{\sqrt{1+ZT_0}} \tag{16}$$

with figure of merit Z and mean air temperature T_0.[12] Load matching of the TEG is done twice, for the optimal case (TEG_{opt}) and the closest real module (Peltron 128A0020). After the source and load matching are executed, the final harvester layout is set (Table IV).

Table III. Properties of the electrical interface

Model	Company	Polarity	$U_{startup}$ in mV	R_{in} in Ω
ECT310	EnOcean	Unipolar	15	2.5
LTC3109	Linear Tech.	Bipolar	±30	5

HARVESTER FIELD TEST AND MODEL VERIFICATION

The source- and load-matched harvester (Table IV) was mounted onto the tunnel wall in the Hugenwald road tunnel from 13 July to 3 August 2011 to show the harvester performance in a worst-case scenario (Fig. 9). A 470-μF storage capacitor and a STM300 transceiver module (EnOcean) were connected to the harvester, forming an autonomous wireless sensor node. The TEG output voltage U_g, the storage capacitor voltage U_C, and the source properties T_{air}, T_{wall}, and v_{air} were measured (Fig. 10) with the data acquisition system (Table I). Due to the source and load matching, the harvester accumulated E_m = 70 mJ of electrical energy per day. The transceiver module consumes 200 μJ of electrical energy for one transmission of 15 bytes (7 data bytes—node ID, temperature value, and storage voltage value). Hence, 415 radio frequency (RF) signals were sent per day. Due to the ultralow startup voltage of the DC/DC converter, the harvester started operating at a total temperature difference of only ΔT = 1.2 K.

The transient model calculates the TEG temperature difference ΔT_g and the electrical energy from the measured source properties total temperature difference ΔT (Fig. 10) and air velocity v_{air}. The FFT uses the mean values of thermal resistance (K_{mean} = 3.2 K/W in Table IV) and cutoff frequency. As these quantities vary with the air velocity throughout the measurement, i.e., K_{max} = 9.1 K/W and K_{min} = 2.3 K/W, the FFT produces a maximum error of 13.8% between modeled and measured ΔT_g. For the energy output calculation, a serious problem

Table IV. Thermal and electrical interfaces (Fischer ickpen45w, EnOcean ECT310) matched to the source and TEG matched to these interfaces

	Thermal Resistance K in K/W		Electrical Resistance R in Ω
Thermal source	air/tnl	air/bld	air/tnl and air/bld
Source matching	3.2	6.2	2.5
Thermal/electrical loads	ickpen45w	ickpen45w	ECT310
Load matching optimal	4.2	8.1	1.9
TEG_{opt}	TEG_{opt}	TEG_{opt}	TEG_{opt}
Load matching real	4		3.5
TEG_{real}	128A0020		128A0020

Load matching of the TEG is presented for the optimal case (TEG_{opt}) and a real TEG module (Peltron 128A0020, T_0 = 294.4 K from Fig. 3).

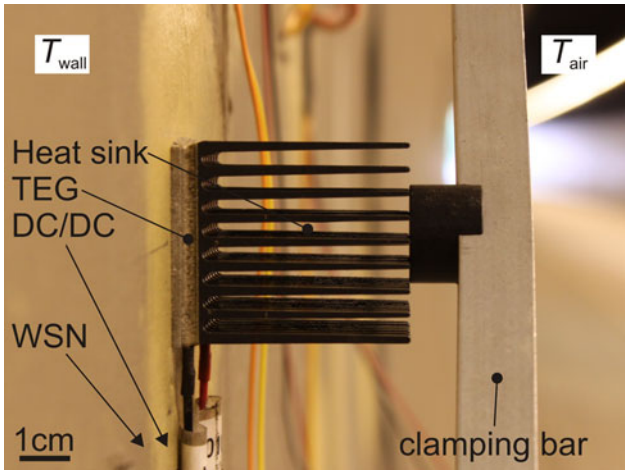

Fig. 9. Source- and load-matched harvester (heat sink, TEG, DC/DC converter) powering the wireless sensor node (WSN) in the tunnel field test.

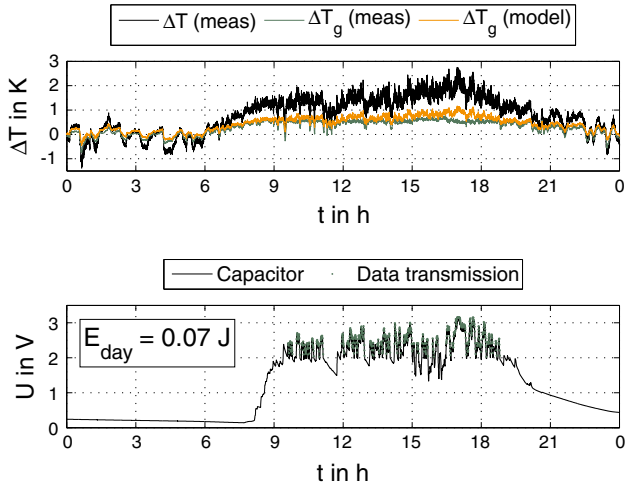

Fig. 10. Source- and load-matched harvester supplying a wireless sensor node with power in the tunnel field test on day 12. Top: temperature differences ΔT between air and wall (total), and at the TEG as measured and calculated by the model. Bottom: voltage at the storage capacitor of the sensor node. The harvested energy of 0.07 J enables 415 data transmissions per day using only the positive half-wave of ΔT.

is the variable input resistance of the DC/DC converter. The model uses the datasheet value, but in the measurement, this electrical resistance varies significantly in the on-state (9–21 h in the upper part of Fig. 10). Therefore, the model predicts an electrical energy of E_{model} = 537 mJ per day.

CONCLUSIONS

The ambient temperature gradient was examined in two simultaneous field measurements, revealing mean absolute temperature differences of 1.2 K and 2.2 K, a 1 mHz cutoff frequency of the wall, and forced convection conditions of 1.15 m/s in the tunnel and 0.28 m/s at the building. Based on these source properties, source matching of the harvester interfaces was performed: The pin fin heat sink ickpen45w has a cutoff frequency 2.5 times greater than the source. The DC/DC converter ECT310 starts operating at 1.2 K source temperature difference. The thermal interface was characterized by heat transfer coefficient measurements, simulations, and analytical means. Load matching of the TEG to the interfaces yielded the 128A0020 as TEG. In a worst-case field test at the tunnel wall, the source- and load-matched harvester still converted 70 mJ of electrical energy per day. The harvester successfully powered a wireless sensor node transmitting 415 RF signals per day. An analytical model for the time-dependent output power of the harvester was introduced. The model predicted the temperature difference at the TEG correctly. The energy calculation failed because the input resistance of the DC/DC converter varied considerably during operation. For model verification, it should be replaced by a constant electrical load resistance. Future work will focus on improving airflow through the heat sink to increase convective heat transfer and the development of a bipolar DC/DC step-up converter

with $U_{\text{startup}} < 30$ mV to cope with both polarities of ΔT.

ACKNOWLEDGEMENTS

We gratefully thank the Federal Ministry of Education and Research (BMBF) and VDI Technologiezentrum GmbH for financial support of the AISIS Project under Grant No. FK 13N9605.

REFERENCES

1. J.M.W. Brownjohn, *Philos. Trans. R. Soc.* 365, 589 (2007).
2. S. Roundy, P.K. Wright, and J.M. Rabaey, *Energy Scavenging for Wireless Sensor Networks* (Boston: Kluwer Academic, 2003).
3. J. Henderson, *Proc. of the 14th Intersociety Energy Conversion Engineering Conference* (1979), p. 1835.
4. J.W. Stevens, *Energy Convers. Manag.* 42, 709 (2001).
5. K. Matsuura and D.M. Rowe, *Handbook of Thermoelectrics*, ed. D.M. Rowe (Boca Raton: CRC, 1995), p. 573.
6. E. Lawrence and G. Snyder, *Proc. of the 21st International Conference on Thermoelectrics* (2002), pp. 446–449. doi: 10.1109/ICT.2002.1190357.
7. Y. Meydbray, R. Singh, and A. Shakouri, *Proc. of the 24th International Conference on Thermoelectrics* (2005), pp. 348–351. doi:10.1109/ICT.2005.1519958.
8. F.P. Incropera, D.P. DeWitt, T.L. Bergman, and A.S. Lavine, *Fundamentals of Heat and Mass Transfer*, 6th ed. (Hoboken: Wiley, 2007).
9. K.K. Sikka, K.E. Torrance, C.U. Scholler, and P.I. Salanova, *IEEE Trans. Compon. Packag. Technol.* (2002). doi:10.1109/TCAPT.2002.1010019.
10. Verein Deutscher Ingenieure, VDI-Wärmeatlas (Springer, Berlin, 2006).
11. J.M. Damaschke, *IEEE Trans. Ind. Appl.* 33, 5 (1997).
12. M. Freunek, *Untersuchung der Thermoelektrik zur Energieversorgung autarker Systeme* (Tönning: Der andere Verlag, 2010).